THE JOURNAL OF PHYSICAL CHEMISTRY C

Article

Cite This: J. Phys. Chem. C 2018, 122, 21703−21717

pubs.acs.org/JPCC

Raman Spectrum of the Organic−Inorganic Halide Perovskite $CH_3NH_3PbI_3$ from First Principles and High-Resolution Low-Temperature Raman Measurements

Miguel A. Pérez-Osorio,[†] Qianqian Lin,[‡,§] Richard T. Phillips,[∥] Rebecca L. Milot,[‡] Laura M. Herz,[‡] Michael B. Johnston,[‡] and Feliciano Giustino*[,†,⊥]

[†]Department of Materials, University of Oxford, Parks Road, Oxford OX1 3PH, United Kingdom

[‡]Clarendon Laboratory, Department of Physics, University of Oxford, Parks Road, Oxford OX1 3PU, United Kingdom

[§]School of Physics and Technology, Wuhan University, Wuhan 430072, P. R. China

[∥]Cavendish Laboratory, Madingley Road, Cambridge CB3 0HE, United Kingdom

[⊥]Department of Materials Science and Engineering, Cornell University, Ithaca, New York 14853, United States

ABSTRACT: We investigate the Raman spectrum of the low-temperature orthorhombic phase of the organic−inorganic halide perovskite $CH_3NH_3PbI_3$, by combining first-principles calculations with high-resolution low-temperature Raman measurements. We find good agreement between theory and experiment and successfully assign each of the Raman peaks to the underlying vibrational modes. In the low-frequency spectral range (below 60 cm^{-1}), we assign the prominent Raman signals at 26, 32, 42, and 49 cm^{-1} to the Pb−I−Pb bending modes with either A_g or B_{2g} symmetry and the signal at 58 cm^{-1} to the librational mode of the organic cation. Owing to their significant intensity, we propose that these peaks can serve as clear markers of the vibrations of the $[PbI_3]^-$ network and of the $CH_3NH_3^+$ cations in this perovskite, respectively. In particular, the ratios of the intensities of these peaks might be used to monitor possible deviations from the ideal stoichiometry of $CH_3NH_3PbI_3$.

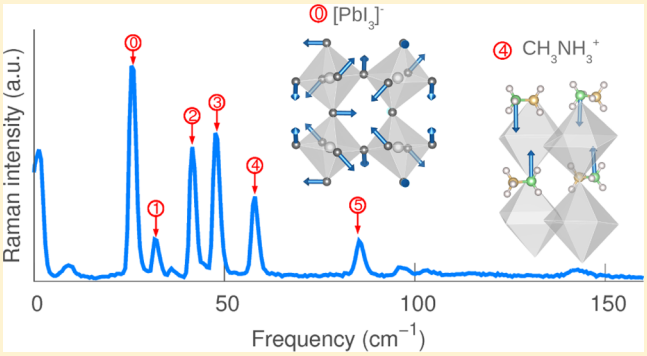

1. INTRODUCTION

Organic−inorganic lead halide perovskites have emerged as promising new materials for high-performance photovoltaics, enabling solution-processable solar cells with certified power conversion efficiency in excess of 22%.[1−5] The prototypical halide perovskite $CH_3NH_3PbI_3$, abbreviated $MAPbI_3$ hereafter, exhibits three polymorphs as a function of temperature.[6−8] It crystallizes in an orthorhombic *Pnma* structure below 162.2 K; between 162.2 and 327.4 K, it adopts an *I*4/*mcm* tetragonal structure; and above 327.4 K, the system stabilizes in a cubic $Pm\bar{3}m$ structure. $MAPbI_3$ exhibits a direct band gap of 1.6 eV and a high absorption coefficient across the visible spectrum.[9,10] The charge carriers exhibit low effective masses, resulting in relatively high mobilities for solution-processable materials, around 50 $cm^2\ V^{-1}\ s^{-1}$.[11−13] The recombination rate of the carriers is also very low, leading to very long diffusion lengths in the micron scale.[11]

The vibrational properties of $MAPbI_3$ and its related compounds have been the subject of numerous investigations,[14−19] as they underpin electron−phonon interactions,[11,20,21] dielectric screening,[22] heat transport, and elastic properties.[23−26] In particular, Raman spectroscopy can be used to identify the symmetry of lattice vibrations,[27,28] to investigate the temperature and pressure phase diagrams of these systems[29−31] and their degree of crystallinity,[32] as well as monitor structural changes in mixed halide perovskites.[17] Raman spectroscopy can also be employed to monitor the stability of halide perovskites during their operation in solar cells.[33] These possibilities provide strong incentives for a detailed characterization of the Raman peaks in these systems.

First-principles calculations along with experiments have shown that the lattice vibrations of $MAPbI_3$ can be classified into three distinct groups: internal vibrations of the organic MA cations, with frequencies ranging between 300 and 3200 cm^{-1}; libration and spinning modes of these cations, with frequencies in the range 60−180 cm^{-1}; and internal vibrations of the inorganic PbI_3 network, with frequencies below 120 cm^{-1}.[16,18,34] The character and symmetry of these vibrational modes have been analyzed in detail in ref 34. In the same work, a large LO−TO splitting of 50 cm^{-1} was predicted for one of the low-frequency Pb−I stretching modes, and this splitting was confirmed by subsequent experiments.[20,35]

The Raman and infrared (IR) spectra of $MAPbI_3$ have been measured by several groups.[16−19,34−36] In most of the IR

Received: May 16, 2018
Revised: August 8, 2018
Published: September 5, 2018

DOI: 10.1021/acs.jpcc.8b04669
J. Phys. Chem. C 2018, 122, 21703−21717

experiments, the degradation of $MAPbI_3$ was avoided by keeping the samples protected from moisture. In the case of Raman measurements, the experiment is more challenging because the perovskite may also degrade as a result of the thermal stress induced by the laser beam if above-gap excitation is used.[17,37] The degradation products, such as PbI_2 and methylammonium iodide (MAI), typically yield additional Raman peaks, which complicate the spectral assignment.[17] Measuring the Raman spectrum of the low-temperature orthorhombic phase of $MAPbI_3$ presents an additional experimental challenge of operation at cryogenic temperatures. To the best of our knowledge, there is only one reported Raman spectrum of orthorhombic $MAPbI_3$.[18,38] The Raman spectrum of the orthorhombic phase of $MAPbI_3$ was also studied via first-principles calculations, and the results are in good agreement with experiments.[16,18,38,39] However, a detailed assignment of each individual peak, including their character and symmetry properties, has not yet been reported.

To fill this gap, here, we investigate the Raman spectrum of $MAPbI_3$ in its low-temperature orthorhombic phase. We combine first-principles density functional perturbation theory calculations in conjunction with high-resolution low-temperature Raman measurements on single crystals. We measure the Raman spectrum of $MAPbI_3$ at several temperatures from liquid-helium temperature (4 K) up to 150 K, in the spectral range up to 120 cm^{-1}. By comparing our calculated spectrum with these data, we succeed in assigning each observed Raman peak. We characterize the peaks using the procedure described in ref 34, where the symmetry of each mode was determined via a factor group analysis. In addition, we explore the effects of van der Waals (vdW) forces, spin−orbit coupling (SOC), and lattice anharmonicity.

The manuscript is organized as follows: in Section 2, we describe the experimental methods and the computational setup. In Section 3, we discuss the calculated Raman spectrum of $MAPbI_3$ and the factor group analysis of the vibrational modes. In this section, we also study the sensitivity of the calculated Raman spectrum to vdW interactions, SOC, and anharmonic effects. In Section 4, we discuss the measured low-temperature Raman spectrum of $MAPbI_3$, and in Section 5, we compare theory and experiment. In Section 6, we summarize our work and offer our concluding remarks.

2. METHODS

2.1. Single-Crystal Preparation and Raman Measurements. $CH_3NH_3PbI_3$ perovskite single crystals were prepared via inverse temperature crystallization.[40] Typically, 1.3 M $CH_3NH_3PbI_3$ precursor was prepared by adding 2.3 g of lead iodide (PbI_2) and 0.8 g of methylammonium iodide (MAI) into 3.85 mL of γ-butyrolactone and heated at 90 °C for 2 h with stirring. Then, the precursor solution was filtered with syringe filters (0.22 μm pore size) and transferred to clean containers, which were kept on a stable hot plate and heated at 130 °C for 3 h. Crystals were formed at the bottom of the containers. Finally, the crystals were collected and dried at 60 °C in a glovebox for 2 h (see Figure 1).

Raman scattering was excited and collected through a microscope objective, sampling a spot on the order of 10^{-6} m diameter, on the surface of a bulk crystal mounted in a coldfinger cryostat. Temperatures quoted relate to the measured coldfinger temperature, and any unshielded thermal radiation will increase the temperature of the surface of the sample measured by the Raman experiment; this effect will be the more significant, the lower the temperature. To minimize this (unquantified) problem, a ring of oxygen-free high-conductivity (OFHC) copper was lowered on to the top of the sample and bonded to it with a thin layer of vacuum grease. The OFHC copper ring was itself thermally anchored to the coldfinger with copper braid. Raman scattering was conducted in the hole in the center of the ring. The sample was illuminated with light from a CW Ti:sapphire laser, cleaned by passing it through a diffraction-grating-based tunable filter, and then linearly polarized using a Glan−Thompson prism. The laser wavelength (830 nm) was chosen to ensure that the photon energy fell below the band gap of $CH_3NH_3PbI_3$, thereby minimizing material degradation and background photoluminescence signals. The Raman scattered light was also resolved in linear polarization by a Glan−Thompson prism, dispersed in a triple-grating spectrometer, and detected on a silicon CCD.

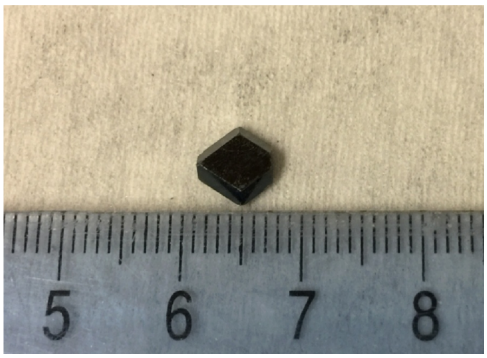

Figure 1. Optical photograph of a typical $CH_3NH_3PbI_3$ crystal obtained in this synthesis.

2.2. Computational Setup. We study the normal modes of vibrations in the low-temperature *Pnma* orthorhombic phase of $MAPbI_3$. The crystal structure was resolved both by neutron and X-ray diffraction experiments.[6,7] In this structure, the MA cations are fully ordered; therefore, the system can be studied using the same computational techniques as for crystalline solids. We calculate structural properties using density functional theory (DFT) and vibrational properties using density functional perturbation theory, as implemented in the planewave pseudopotential package Quantum ESPRESSO.[41] In a previous work by some of us,[42] we showed that the two most popular approximations to the exchange−correlation functional, the generalized-gradient approximation of Perdew, Burke, and Ernzerhof[43] and the local density approximation (LDA),[44] work remarkably well in describing the vibrational properties of $MAPbI_3$. On the basis of these findings, here, we proceed with the LDA exchange and correlation. The core−valence electron interaction is described by means of norm-conserving pseudopotentials, including 5d semicore states for Pb.[45] The wave functions are represented by planewave basis sets with a kinetic energy cutoff of 100 Ry, and the Brillouin zone is sampled using a 4 × 4 × 4 Monkhorst−Pack grid. The orthorhombic unit cell of $MAPbI_3$ is optimized starting from the experimental lattice parameters reported in ref 6. The vibrational eigenmodes and frequencies are computed at the Γ point.

Within the Placzek approximation, the nonresonant Raman intensity I^k of a vibrational mode k with frequency ω_k is given by[27]

DOI: 10.1021/acs.jpcc.8b04669
J. Phys. Chem. C 2018, 122, 21703−21717

$$I^k \propto \frac{1}{\omega_k}|\mathbf{e}_i \cdot \bar{\alpha}^k \cdot \mathbf{e}_s|^2 \quad (1)$$

where $\mathbf{e}_i$ and $\mathbf{e}_s$ are the polarization vectors of the incoming and scattered photons, respectively. $\bar{\alpha}^k$ is the Raman tensor associated with this mode, and its components α_{ij}^k in Cartesian coordinates are given by[46]

$$\alpha_{ij}^k = \frac{\sqrt{\Omega}}{4\pi} \sum_{I,m} \chi_{ij,Im}^{(1)} \frac{v_{k,Im}}{\sqrt{M_I}} \quad (2)$$

In this equation, Ω is the volume of the unit cell, $\chi_{ij}^{(1)}$ is the first partial derivative of the dielectric polarizability χ_{ij} with respect to the displacement of the atom I along the Cartesian direction m, $v_{k,Im}$ is a normalized vibrational eigenmode, and M_I is the atomic mass. The derivatives $\chi_{ij}^{(1)}$ are evaluated via finite differences.[46]

The nonresonant approximation should be adequate in this case because the laser energy (830 nm) is more than 100 meV away from the absorption edge. In fact, the width of a Raman resonance curve is determined by the imaginary part of the energy denominator, in a second-order perturbative approach to the description of the scattering. In a band picture, this was investigated in detail many years ago for $Al_xGa_{1-x}As$, and the broadening parameters found to be on the order of a few meV for resonances at the $E_0 + \Delta$ gap.[47,48] In that work, the resonance enhancement has fallen by a substantial factor already at 100 meV from the absorption edge, which is similar to the setup used in this manuscript.

The measured Raman spectra are recorded using the horizontal−horizontal (HH) and horizontal−vertical (HV) polarizations of the incident light and analyzer. The total Raman intensity is given by $I = I_{HH} + I_{HV}$. We calculate each component by taking the isotropic average over crystal orientations[49,50]

$$I_{HH}^k = \frac{1}{\omega_k}\left(a_k^2 + \frac{4b_k^2}{45}\right), \quad I_{HV}^k = \frac{1}{\omega_k}\frac{3b_k^2}{45} \quad (3)$$

where

$$a_k = (\alpha_{11}^k + \alpha_{22}^k + \alpha_{33}^k)/3 \quad (4)$$

$$b_k^2 = [(\alpha_{11}^k - \alpha_{22}^k)^2 + (\alpha_{11}^k - \alpha_{33}^k)^2 + (\alpha_{22}^k - \alpha_{33}^k)^2]/2 + 3[(\alpha_{12}^k)^2 + (\alpha_{13}^k)^2 + (\alpha_{23}^k)^2] \quad (5)$$

Our choice of taking the isotropic average relates to the fact that we could not establish the precise orientation of the crystal with respect to the light polarization, as samples were found to crack following thermal cycling. Although we could not resolve the orientation of the crystal, we determine the Raman activity of the normal modes for several orientations of a single crystal of $MAPbI_3$, in backscattering geometry. We achieve this by considering the symmetry of the Raman tensors and eq 1. We then confirm our predictions by explicitly calculating the Raman spectra for the different backscattering configurations considered here. Our results are presented in Appendix A. To investigate the sensitivity of the Raman spectrum to vdW interactions, SOC, and anharmonicity, we correct the vibrational frequencies using the data of our previous work, ref 42, and we recompute the spectra in each case. We do not correct the eigenmodes as we have already shown that the variations are very small.[42] Because different vdW schemes yield similar corrections to the vibrational eigenfrequencies of $MAPbI_3$, we here focus on the results obtained via the Grimme-D2 approximation.[51,52] For completeness, we also recalculate IR intensities, using the same method as in ref 34.

3. RESULTS AND DISCUSSION

3.1. Structure. Figure 2 shows a polyhedron-ball-and-stick model of the optimized orthorhombic crystal structure of $MAPbI_3$. The primitive unit cell contains 48 atoms: 4 Pb atoms, 12 I atoms, and 4 MA cations. The Pb and I atoms form a corner-sharing network of octahedra, with the Pb atoms at the center of each octahedron and the I atoms at the corners. The MA cations occupy the cavities formed by the PbI_3 network.

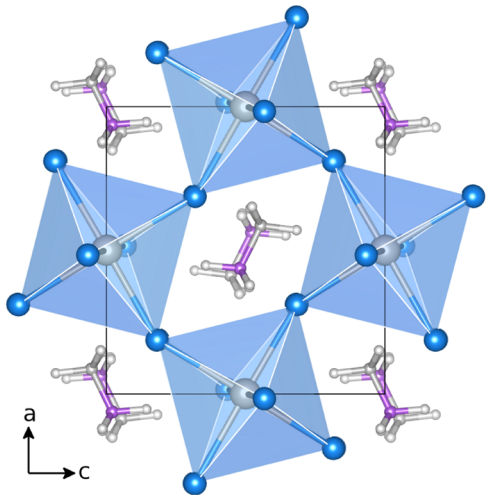

Figure 2. Polyhedron-ball-and-stick model of the optimized structure of the low-temperature orthorhombic phase of $MAPbI_3$, viewed across the *ac* plane of the unit cell. The unit cell is indicated by the black lines. The Pb and I atoms are in gray and blue, respectively, whereas the C, N, and H atoms of the MA cations are in gray, purple, and white, respectively.

The average of the calculated Pb−I bond lengths and of the apical and equatorial Pb−I−Pb bond angles are 3.19 Å, 158.7°, and 149.5°, respectively. These values compare very well with the corresponding experimental values of 3.18 Å, 161.9°, and 150.7°, respectively. The average C−N, C−H, and N−H bond lengths in the MA cations are 1.10, 1.06, and 1.45 Å, respectively. Also, these values are in good agreement with the corresponding experimental values of 1.1, 1.0, and 1.57 Å, respectively.

3.2. Normal Mode Analysis. A visual inspection of the calculated eigendisplacements of $MAPbI_3$ suggests that they can be classified as vibrations of the MA cations, vibrations of the PbI_3 network, or mixed modes. To clarify the nature of the normal modes on a more quantitative ground, we perform a decomposition following the procedure of ref 34. In this procedure, the normal modes are decomposed into rigid rotations of the PbI_3 octahedra, internal vibrations of the inorganic network, rigid modes of the MA cations (including translation, spinning, and libration), and internal vibrations of the cations. The total and the partial vibrational density of states (vDOS) are shown in Figure 3.

The frequencies of the calculated vibrational modes extend up to 3200 cm^{-1}. We observe that the normal modes with frequencies between 300 and 3100 cm^{-1} correspond to pure internal vibrations of the MA cations. In the low-frequency

DOI: 10.1021/acs.jpcc.8b04669
J. Phys. Chem. C 2018, 122, 21703−21717

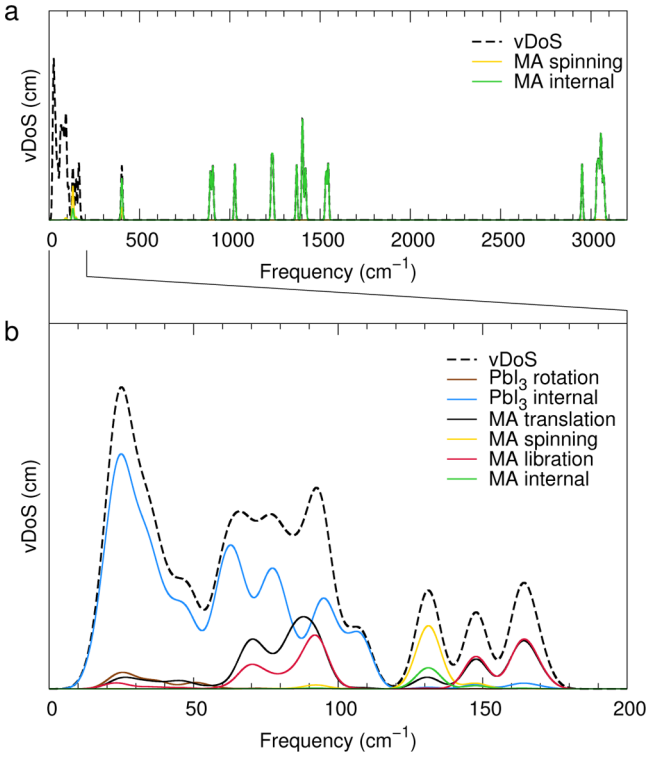

Figure 3. (a) Calculated total and partial vibrational density of states (vDOS) of the low-temperature orthorhombic phase of $MAPbI_3$. (b) Detail of the vDOS in the low-frequency region. The dashed black curve indicates the total vDOS. The vibrational modes are decomposed into rigid rotations and internal vibrations of the PbI_3 octahedra (brown and blue curves, respectively) and into translation (solid black curve), spinning (yellow curve), and libration (red curve) of the MA cations, and internal vibrations (green curve) of these cations. A Gaussian smearing of 5 cm^{-1} has been applied to all curves.

region, the normal modes with frequencies between 140 and 180 cm^{-1} are combinations of librations and translations of the MA cations. The distinct feature at 130 cm^{-1} is associated primarily with MA spinning around the C−N axis. Between 65 and 120 cm^{-1}, the normal modes are either libration/translation modes of the MA cations or internal vibrations of the PbI_3 network. In contrast, the normal modes appearing below 65 cm^{-1} are found to be dominated by internal vibration of the PbI_3 network. These results are fully consistent with previous work.[18,34,39]

3.2.1. Symmetry and Character of the Normal Modes. Because the normal modes of $MAPbI_3$ can be classified as vibrations of the PbI_3 network or vibrations of the MA cations, we study the symmetry of these two families of normal modes using a separate factor group analysis in each case.[53−55]

We start with the normal modes of the PbI_3 network. In this case, we consider that orthorhombic $MAPbI_3$ belongs to the *Pnma* space group. We identify 48 normal modes as vibrations of the PbI_3 network (3 acoustic and 45 optical modes), consistent with the number of Pb and I atoms in the unit cell. The optical modes admit the following symmetry representations: $\Gamma = 7B_{1u} + 6B_{2u} + 7B_{3u} + 5A_g + 4B_{1g} + 5B_{2g} + 4B_{3g} + 7A_u$. Among these representations, the g type (gerade, even) contains inversion symmetry, whereas the u type (ungerade, odd) does not. For each of the normal modes, we assign the symmetry by checking their transformation under the symmetry operations of each irreducible representation. The resulting assignment is reported in Table 1. In the same table, we indicate the character of each mode in terms of Pb−I stretching, Pb−I−Pb bending, and Pb−I−Pb rocking motion.

In the case of the MA cations, we identify 4 spinning modes, 20 normal modes that are combinations of translations and librations, and 72 internal vibrations. If we cumulate the fractions of libration and translation in each mode, we obtain a total of 12 translations and 8 librations, consistent with the fact that there are 4 cations in the unit cell. The calculated frequencies of these modes and their character are reported in Table 2.

By performing a visual inspection of the internal vibrations of the MA cations in $MAPbI_3$, we note that the individual atomic displacements largely resemble those of isolated MA cations. Furthermore, we find that the modes of the MA cations appear grouped in quadruples of nearly degenerate frequencies. This suggests that although the vibrations of the four MA cations in $MAPbI_3$ lead to collective vibrations (e.g., in-phase and out-of-phase modes) the inter-cation coupling is small. On the basis of this observation, we proceed to discussing the symmetry and character of the internal vibrations of MA using the isolated cation as a reference. The internal vibrations of an isolated MA cation admit the following symmetry representations: $A_2 + 5A_1 + 6E$, with the E modes being doubly degenerate. By combining the symmetry and character of these normal modes, they can further be described as symmetric or asymmetric CH_3- and NH_3-deformation modes, symmetric C−N stretching modes, symmetric or asymmetric C−H and N−H stretching modes, and asymmetric CH_3-NH_3 rocking modes. This characterization is reported in Table 3. For clarity, we report the average frequency of each quadruple of nearly degenerate modes.

The symmetry of each normal mode dictates its Raman and IR activity.[27,34,53,56] In the case of the PbI_3 network, the normal modes with A_g, B_{1g}, B_{2g}, and B_{3g} symmetries are predicted to be Raman-active, whereas those with B_{1u}, B_{2u}, and B_{3u} symmetries are predicted to be IR-active. None of the modes is at the same time Raman- and IR-active because orthorhombic $MAPbI_3$ is centrosymmetric.[27] The A_u modes are expected to be silent.

In the case of the MA cations, our choice of focusing on the individual molecules does not allow us to predict Raman and IR activity by symmetry. Indeed, the prediction of which modes will be active requires the use of the symmetries of the complete structure. This analysis was performed in ref 57, where the authors showed that the symmetry of these modes can be described as follows: $\Gamma = 14B_{1u} + 10B_{2u} + 14B_{3u} + 14A_g + 10B_{1g} + 14B_{2g} + 10B_{3g} + 10A_u$. As for the PbI_3 network, the u modes will be IR-active, the g modes will be Raman-active, and the A_u modes will be silent. Because our main focus is the vibrational modes of the PbI_3 network, here, we do not repeat the symmetry analysis of ref 57 and we simply calculate explicitly the Raman and IR intensities of these modes. The data are reported in Table 3.

3.3. Calculated Raman and IR Intensities. The calculated Raman and IR intensities of the normal modes of $MAPbI_3$ are reported in Tables 1−3. We first discuss our results for the PbI_3 network (Table 1). We note that the calculated Raman intensities of several normal modes with A_g, B_{1g}, B_{2g}, and B_{3g} symmetries are sizeable, whereas the IR intensities of the same modes are negligible. Similarly, the modes with B_{1u}, B_{2u}, and B_{3u} symmetries exhibit negligible Raman intensities but nonzero IR intensities. The A_u modes do not exhibit any significant Raman or IR intensity. These

DOI: 10.1021/acs.jpcc.8b04669
J. Phys. Chem. C 2018, 122, 21703−21717

Table 1. Symmetry, Character, Frequency, and Predicted Raman Activity of the Calculated Vibrational Modes of the PbI_3 Network in $MAPbI_3$[a]

mode no.	symm.	character	active	freq. (cm^{-1})	Raman intensity ($Å^5/kg$) × 10^8	IR intensity [$(D/Å)^2/kg$]
1	B_{1u}			0.0		
2	B_{2u}			0.0		
3	B_{3u}			0.0		
4	A_u	Pb−I−Pb bend	silent	16.5		
5	B_{2u}		IR	19.6		0.2
6	B_{1u}	Pb−I−Pb rock	IR	22.1		0.4
7	B_{1g}	Pb−I−Pb rock	R	22.9		
8	B_{3u}	Pb−I−Pb bend	IR	23.3		0.2
9	A_u		silent	23.4		
10	B_{3g}	Pb−I−Pb rock	Raman	23.6		
11	A_g	Pb−I−Pb rock	R	24.8	0.8	
12	A_u		silent	25.6		
13	A_u	Pb−I−Pb rock	silent	26.5		
14	B_{2u}	Pb−I−Pb rock	IR	26.6		0.4
15	B_{1u}		IR	26.6		0.1
16	B_{2g}	Pb−I−Pb rock	R	26.7	0.5	
17	A_g	Pb−I−Pb rock	R	29.9	3.6	
18	B_{2u}	Pb−I−Pb bend	IR	31.6		1.8
19	B_{3u}	Pb−I−Pb rock	IR	31.9		1.6
20	B_{3u}	Pb−I−Pb rock	IR	33.4		0.1
21	B_{2g}	Pb−I−Pb bend	R	34.6	0.7	
22	B_{1u}	Pb−I−Pb rock	IR	36.0		1.4
23	B_{1g}	Pb−I−Pb bend	R	37.1		
24	B_{2g}		R	40.4	3.5	
25	A_g	Pb−I−Pb bend	R	41.3	15.6	
26	B_{1u}	Pb−I−Pb bend	IR	46.1		0.5
27	B_{3g}	Pb−I−Pb bend	R	46.7		
28	B_{3u}		IR	50.3		1.5
29	A_g	Pb−I−Pb bend	R	51.5	6.0	
30	B_{2g}	Pb−I−Pb bend	R	58.1	5.9	
31	B_{2u}	Pb−I stretch	IR	58.2		7.2
32	A_u	Pb−I stretch	silent	59.3		
33	B_{1u}	Pb−I stretch	IR	61.1		16.2
34	B_{3u}	Pb−I stretch	IR	63.2		16.4
35	A_u	Pb−I stretch	silent	63.5		
36	B_{2u}	Pb−I stretch	IR	66.4		10.6
41	B_{1u}	Pb−I−Pb bend	IR	74.7		0.2
42	B_{3u}	Pb−I−Pb bend	IR	75.5		0.1
43	A_u	Pb−I−Pb bend	silent	77.4		
44	B_{2u}		IR	77.6		0.9
45	B_{1u}	Pb−I−Pb bend	IR	79.9		0.9
46	B_{3u}		IR	81.2		0.4
53	B_{3g}	Pb−I stretch	R	93.4	1.8	
54	B_{1g}	Pb−I stretch	R	93.9	0.7	
56	A_g	Pb−I stretch	R	95.2	1.0	
58	B_{1g}	Pb−I stretch	R	101.3	0.3	
59	B_{2g}	Pb−I stretch	R	106.8		
60	B_{3g}	Pb−I stretch	R	108.0		

[a]We also report the calculated IR intensity for completeness. The labels "R" and "IR" indicate modes that are expected to be Raman-active or IR-active by symmetry. We also report the Raman and IR intensities calculated from first principles. Whenever the Raman or IR intensity is not indicated, the corresponding value is smaller than 0.1 × 10^8 $Å^5/kg$ or 0.1 $(D/Å)^2/kg$, respectively.

calculations confirm our predictions in Section 3.2.1. A schematic representation of the modes with the largest Raman intensity is shown in Figure 4; these modes correspond to Pb−I−Pb rocking motion, Pb−I−Pb bending, and Pb−I stretching, respectively.

The vibrations corresponding to rigid-body motion of the MA cations with the largest Raman intensity are shown in Figure 5. These modes correspond to spinning and libration of the cations. The corresponding Raman and IR intensities are reported in Table 2. Also, in this case, we observe that the modes are either Raman- or IR-active, but not both, in line with the fact that orthorhombic $MAPbI_3$ is centrosymmetric.

Similar considerations apply to the internal vibrations of the MA cations. The calculated Raman and IR intensities of these

DOI: 10.1021/acs.jpcc.8b04669
J. Phys. Chem. C 2018, 122, 21703−21717

Table 2. Character, Frequency, and Calculated Raman Intensity of the Vibrational Modes Corresponding to the Rigid-Body Motion of the MA Cations in $MAPbI_3$[a]

mode no.	character	frequency (cm^{-1})	Raman intensity ($Å^5/kg$) × 10^8	IR intensity $[(D/Å)^2/kg]$
37	libr/transl	68.5		
38	libr/transl	69.0	0.4	
39	libr/transl	69.9		
40	libr/transl	73.9	2.7	
47	translation	84.8		3.2
48	libr/transl	84.9	0.2	
49	translation	86.3		1.9
50	libr/transl	89.6		
51	libr/transl	92.9	1.0	
52	libr/transl	93.3		0.2
55	libr/transl	94.7	0.4	
57	libr/transl	95.3		
61	spin	124.7		1.0
62	spin	125.9	0.8	
63	spin	127.4	0.3	
64	spin	128.6		
65	libr/transl	150.3		8.6
66	libr/transl	153.2	0.5	
67	libr/transl	153.5	0.1	
68	libr/transl	164.7	10.8	
69	libr/transl	165.6	1.9	
70	libr/transl	165.9		9.8
71	libr/transl	166.9	0.7	
72	libr/transl	169.3		1.1

[a]We also report the IR intensities for completeness. We distinguish spinning, libration, and translations based on the decomposition shown in Figure 2. Modes of mixed character correspond to vibrations where the contributions of different components have similar weights in Figure 2. Whenever the Raman or IR intensity is not indicated, the corresponding value is smaller than 0.1 × 10^8 $Å^5/kg$ or 0.1 $(D/Å)^2/kg$, respectively.

modes are reported in Table 3, and a schematic representation of the atomic displacements is shown in Figure 6.

3.4. Calculated Raman Spectrum. The calculated Raman spectrum of $MAPbI_3$ is shown in Figure 7. Going from high frequency to low frequency, we first encounter an intense Raman peak at 3048 cm^{-1}, which corresponds to N−H stretching modes with molecular symmetry A_1. The small peak on the right, at 3062 cm^{-1}, is assigned to N−H stretching modes with E symmetry, whereas the small peak on the left, at 3046 cm^{-1}, arises from C−H stretching modes with E symmetry. The Raman peak at 2952 cm^{-1} originates from a C−H stretching mode with A_1 molecular symmetry.

In the central region of the spectrum in Figure 7, the peak at 1544 cm^{-1} is assigned to NH_3 deformation modes with E symmetry. The peak at 1419 cm^{-1} is a NH_3 deformation with A_1 molecular symmetry, whereas the shoulder on the left at 1403 cm^{-1} arises from CH_3 deformations with E symmetry. Proceeding toward lower frequency, the peaks at 1239 and 906 cm^{-1} are CH_3NH_3 rocking modes with E symmetry, whereas the peak centered at 1029 cm^{-1} is assigned to C−N stretching modes with A_1 symmetry. At even lower frequency, there is a small peak at 401 cm^{-1}, which is barely discernible in Figure 7; this feature corresponds to torsional modes of the MA cations. We emphasize that the present symmetry assignment for the internal vibrations of MA relates to the local symmetry of each cation, as opposed to the symmetry of the entire crystal.

In the low-frequency region, we find that the peak at 164 cm^{-1}, showing a significant Raman intensity, and the small peak on its left side, at 152 cm^{-1}, both correspond to librational modes of the MA cations. At lower frequencies, the small feature at 125 cm^{-1} is assigned to spinning modes of the MA cations. Moving to lower frequencies, we find that the peak at 93 cm^{-1} stems from librational modes of the MA cations and internal vibration modes of the PbI_3 network, with B_{3g} and A_g symmetries, respectively. The peak at 74 cm^{-1} primarily corresponds to librational modes of the MA cations, whereas the peaks at 58 and 52 cm^{-1} are assigned to Pb−I−Pb bending modes with B_{2g} and A_g symmetries, respectively. Further down, the peak at 41 cm^{-1} arises primarily from Pb−I−Pb bending motion with A_g symmetry but also comprises a component of Pb−I−Pb bending with B_{2g} symmetry. The

Table 3. Symmetry, Character, Frequency, and Raman Intensity of the Internal Vibrations of the MA Cations in $MAPbI_3$[a]

mode no.	molecular symmetry	character	frequency (cm^{-1})	Raman intensity ($Å^5/kg$) × 10^8	IR intensity $[(D/Å)^2/kg]$
73−76	A_2	sym. torsion	401	0.1	0.4
77−80	E	asym. CH_3NH_3 rock	893	0.2	9.3
81−84	E	asym. CH_3NH_3 rock	906	0.8	6.3
85−88	A_1	sym. C−N stretch	1029	0.3	0.5
89−92	E	asym. CH_3NH_3 rock	1231	0.5	0.6
93−96	E	asym. CH_3NH_3 rock	1239	0.4	0.3
97−100	A_1	sym. CH_3 deformation	1370	0.5	0.8
101−108	E	asym. CH_3 deformation	1403	0.8	2.4
109−112	A_1	sym. NH_3 deformation	1419	4.2	4.5
113−116	E	asym. NH_3 deformation	1533	0.1	3.0
117−120	E	asym. NH_3 deformation	1544	2.1	1.6
121−124	A_1	sym. C−H stretch	2952	10.9	0.2
125−128	E	asym. C−H stretch	3035	1.4	21.8
129−132	E	asym. C−H stretch	3046	6.2	103.2
133−136	A_1	sym. N−H stretch	3048	40.9	16.5
137−144	E	asym. N−H stretch	3062	8.6	115.4

[a]We also report the calculated IR intensities for completeness. The frequencies and intensities are averaged over nearly degenerate modes. Whenever the Raman or IR intensity is not indicated, the corresponding value is smaller than 0.01 × 10^8 $Å^5/kg$ or 0.1 $(D/Å)^2/kg$, respectively.

DOI: 10.1021/acs.jpcc.8b04669
J. Phys. Chem. C 2018, 122, 21703−21717

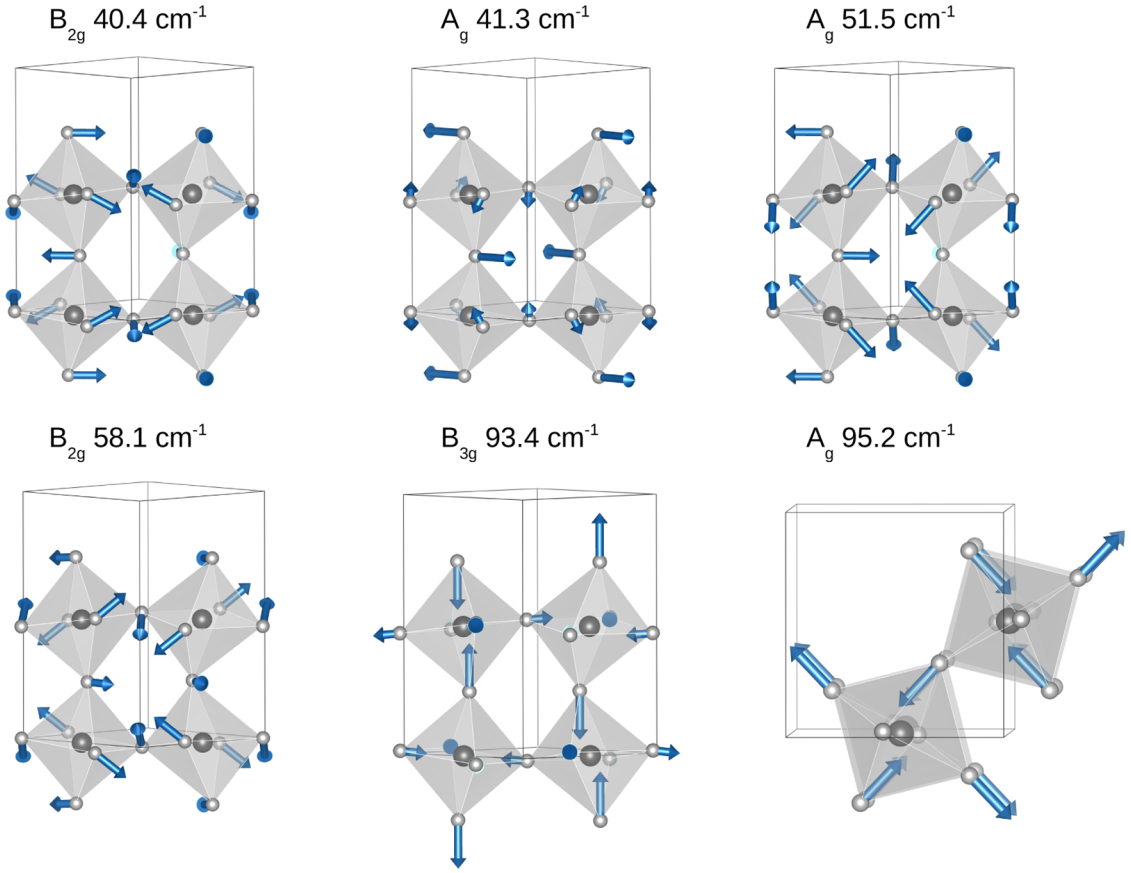

Figure 4. Schematic representation of the most important Raman-active modes of the PbI_3 network in $MAPbI_3$. The MA cations, whose contribution to the Raman intensity is negligible, are not shown for clarity. The symmetry and calculated frequency of each normal mode are indicated at the top of the each panel, and the solid black lines indicate the unit cell.

remaining peak at 30 cm^{-1} is attributed to Pb−I−Pb rocking modes with A_g symmetry.

3.5. Sensitivity of Calculated Raman Spectrum to vdW Interactions, SOC, and Anharmonicity. Before comparing our calculated Raman spectrum with our experimental data in Section 5, we investigate the sensitivity of the calculations to the inclusion of vdW interactions, SOC effects, and anharmonicity.

In a recent work by some of us,[42] we investigated the role of vdW interactions, SOC, and anharmonicity in the vibrational properties of $MAPbI_3$. We found that vdW interactions, relativistic effects, and anharmonic corrections have very little impact on the majority of vibrational modes of this perovskite and only introduce small corrections to the normal-mode frequencies, Born effective charge tensors, dielectric constant, and IR spectrum. However, we also found that the spinning modes of the MA cations carry considerable anharmonicity; in fact, anharmonic corrections blue-shift the frequencies of these modes by as much as 35 cm^{-1}. The anharmonic shift of the spinning modes has no impact on the IR spectrum because these modes have almost negligible IR intensities.[34]

Here, we assess the impact of these effects on the Raman spectrum using the frequency shifts determined in ref 42. The Raman spectra computed by including the various corrections are shown in Figure 8. The bottom line (black) is for the uncorrected spectrum calculated using scalar-relativistic LDA; immediately above, we have the spectrum with frequencies corrected by vdW interactions (blue); proceeding upward, we have the spectrum with SOC corrections (red), then SOC and vdW combined together (green); and finally the spectrum with anharmonic corrections (brown).

A close comparison of the spectra reported in Figure 8 indicates that vdW interactions and SOC tend to shift peaks by ±15 cm^{-1}, but we cannot identify any systematic trend. These variations can be considered to lie within the standard DFT error and are comparable to the changes expected when using different pseudopotentials. These results reinforce the notion that vdW interactions do not have any significant impact on the vibrational properties of $MAPbI_3$ and indicate that interaction between the inorganic PbI_3 network and the MA cations is primarily electrostatic in nature.[39,42,58,59] Anharmonic corrections lead to similarly small corrections to the frequencies, with the only exception being the spinning modes of MA. The Raman signal of these modes blue-shifts from 126 to 162 cm^{-1} (Figure 8), but the Raman intensity is so small that the effect is barely noticeable.

4. MEASURED RAMAN SPECTRA OF $MAPbI_3$

In Figure 9, we show the Raman spectra acquired for single crystals of $MAPbI_3$ in the orthorhombic phase. The HV spectrum measured at 4 K shows five peaks between 10 and 70 cm^{-1} and two small features at 85 and 97 cm^{-1}. Additionally, the HH spectrum at 4 K exhibits a further small feature at 9 cm^{-1}. These peaks tend to broaden with increasing temperature, in line with the increasing probability of phonon−phonon scattering, and exhibit a slight red shift on the order of 4 cm^{-1}, which we tentatively attribute to lattice expansion and phonon−phonon interactions. The small peaks at 85 and 97

DOI: 10.1021/acs.jpcc.8b04669
J. Phys. Chem. C 2018, 122, 21703−21717

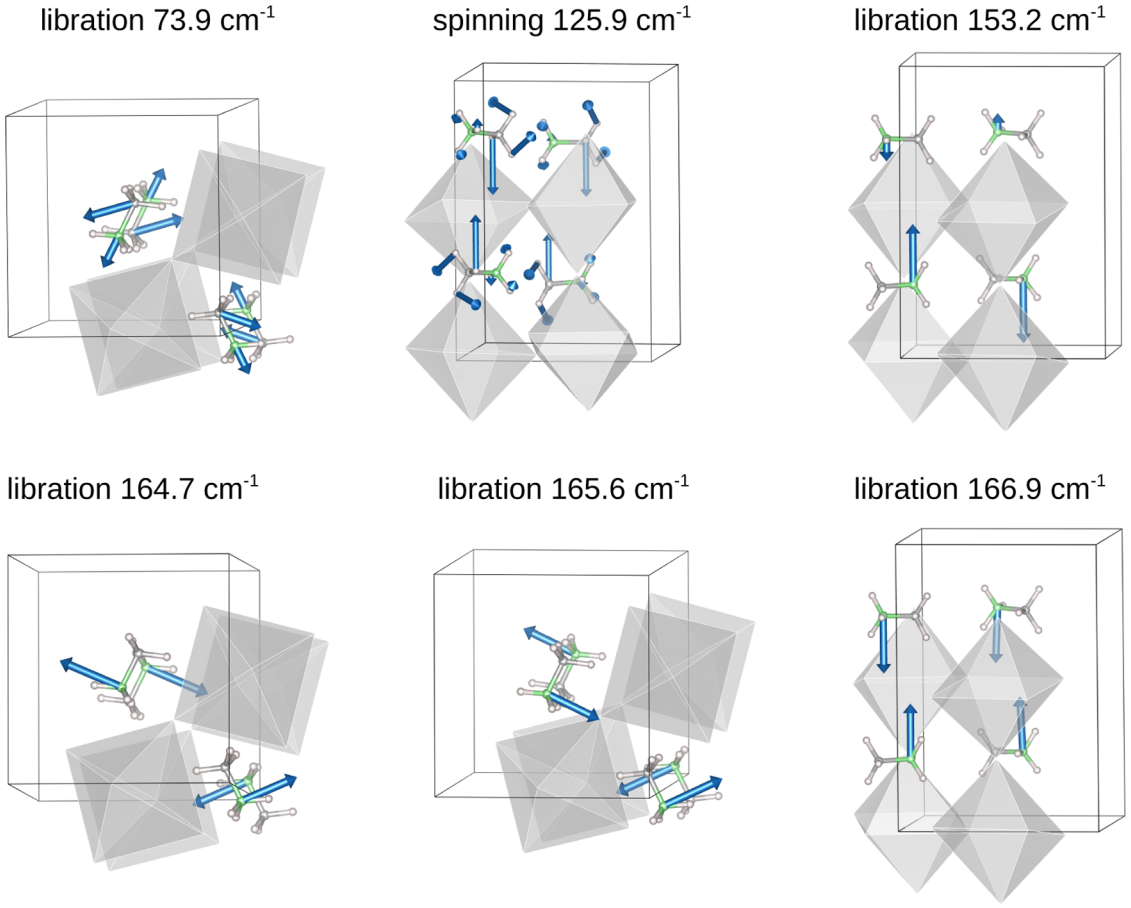

Figure 5. Schematic representation of the libration/translation and spinning modes of the MA cations with the largest calculated Raman intensities. For clarity, we show only the octahedra without the Pb and I atoms, and in the librational modes, only the displacements of the C and N atoms are indicated by arrows. The character and frequency of each mode are reported at the top. We note that all of these modes also include a component of rigid translation of the cations.

cm^{-1} are at the detection limit for the experiment, and one plausible explanation for their progressive disappearance as the temperature is raised is that they vanish into the noise as they broaden at higher temperatures.

Importantly, there are no new features appearing with increasing temperature, and we do not observe peaks around 94 and 110 cm^{-1}, which would indicate the presence of PbI_2.[17] Thus, our data indicate that $MAPbI_3$ is not undergoing degradation during the Raman experiments and the spectra are representative of the pristine material.

5. COMPARISON OF MEASURED AND CALCULATED RAMAN SPECTRA

In Figure 10, we compare the HH and HV Raman spectra measured for $MAPbI_3$ at 4 K with our first-principles calculations. In the calculated spectrum, we include anharmonic corrections, following the discussion in Section 3.5.

Our calculations nicely reproduce the frequency and relative intensity of almost all of the peaks observed in the experiments, for both polarization configurations, except for the measured peak at 142 cm^{-1}. We will come back on this point below. Overall, the good agreement between theory and experiment allows us to proceed with a complete assignment of the measured peaks. Our proposed assignment of the Raman spectrum is indicated in Figure 10 by the dashed black lines. The measured peak at 9 cm^{-1} (labeled as "0" in Figure 10) is assigned to Pb−I−Pb rocking modes with A_g symmetry. The peak at 26 cm^{-1} corresponds to Pb−I−Pb bending modes with A_g symmetry (1), and the small peak next to it, at 32 cm^{-1}, originates from Pb−I−Pb bending modes with B_{2g} symmetry (2). At a slightly higher frequency, the peaks at 42 and 49 cm^{-1} are assigned to Pb−I−Pb bending modes with A_g (3) and B_{2g} (4) symmetries, respectively, whereas the peak at 58 cm^{-1} corresponds to librational modes of the MA cations (5). At even higher frequency, the peak at 85 cm^{-1} is assigned to librational modes of the MA cations as well as to Pb−I stretching modes with B_{3g} symmetry (6), whereas the peak at 97 cm^{-1} stems from Pb−I stretching modes of A_g symmetry (7). In the high-frequency region of the spectrum, the small peak at 142 cm^{-1} (8) is assigned to librational modes of the MA cations. For clarity, these assignments are summarized in Table 4.

Generally speaking, our assignments indicate that the Raman peaks observed below 50 cm^{-1} in the experiments are internal vibrations of the inorganic PbI_3 network, whereas above this frequency, the features at 58 and 142 cm^{-1} correspond to librational modes of the MA cations, and the peak at 85 cm^{-1} is a combination of MA libration and internal vibrations of the inorganic network. Owing to the significant Raman intensities of the peaks at 26, 42, 49, and 58 cm^{-1}, the first three of these peaks could be used as markers of the inorganic PbI_3 network, whereas the last one could serve as a fingerprint of the MA cations. Because these assignments are unambiguous, the ratios

DOI: 10.1021/acs.jpcc.8b04669
J. Phys. Chem. C 2018, 122, 21703−21717

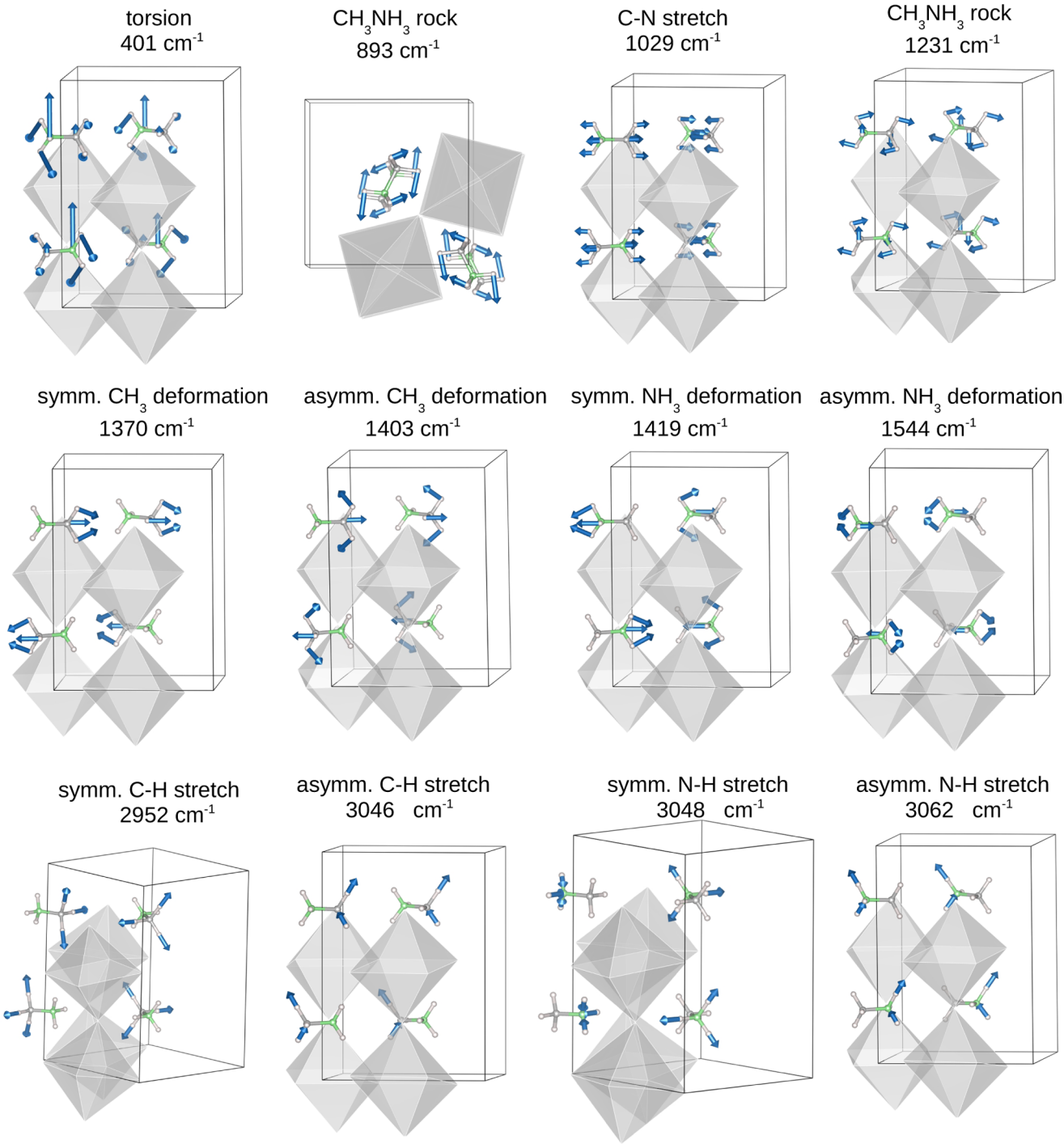

Figure 6. Schematic representation of the internal vibrations of the MA cations in $MAPbI_3$. For each set of normal modes reported in Table 2, we show a schematic representation of the mode with the largest Raman intensity. The mode character and frequency are given at the top of each panel.

of the intensities of PbI_3-related peaks and the MA-related peak could be used to monitor possible deviations from the ideal stoichiometry of $MAPbI_3$, for example, to check sample purity or detect early signs of degradation.

We now comment on the intensity of the Raman peak at 142 cm^{-1}, which we assigned to MA librational and translational modes. As can be seen in Figure 10, our calculations yield an intensity that is significantly larger than that in experiments. We notice that Brivio et al.[18] also reported an overestimation of the intensity of this Raman peak by calculations. In a previous work by some of us,[34] we performed a similar comparison between theory and experiment for IR spectra, and we also found that our calculations significantly overestimate the IR intensity of the same peak. Therefore, it seems that we consistently overestimate the Raman and IR activities of the MA librational/translational modes. The origin of this discrepancy remains unclear. A possible explanation may be that vdW interactions, SOC, and anharmonicity may affect the Raman intensities of these modes (as opposed to their frequencies). However, it has previously been shown that

DOI: 10.1021/acs.jpcc.8b04669
J. Phys. Chem. C 2018, 122, 21703−21717

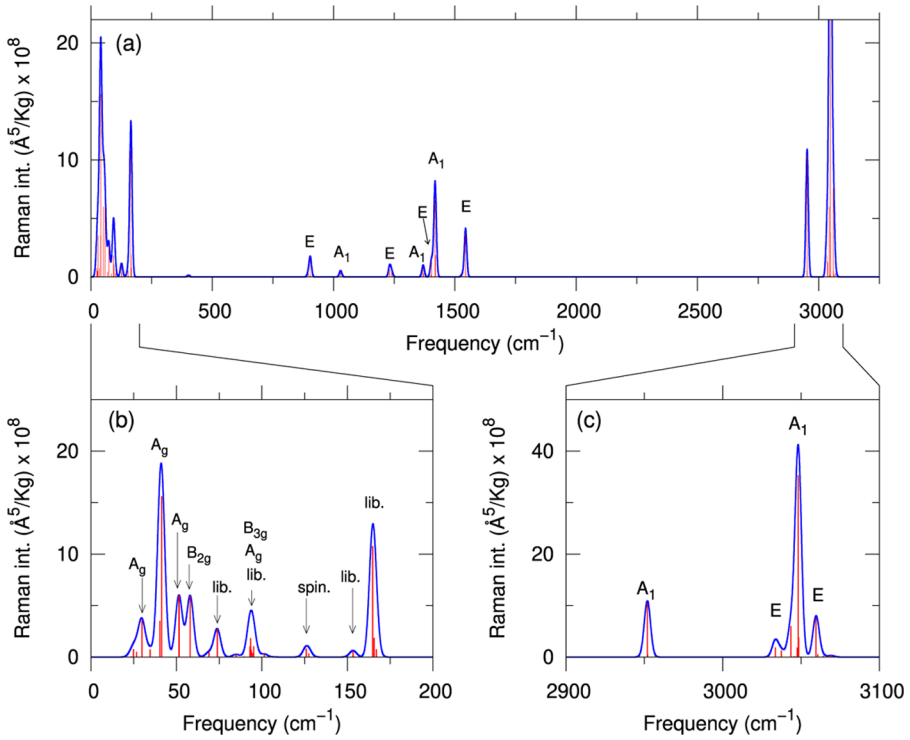

Figure 7. (a) Calculated Raman spectrum of $MAPbI_3$ in the orthorhombic structure. (b, c) Details of the calculated Raman spectrum in the low- and high-frequency regions, respectively. The red sticks indicate the calculated Raman intensities of the normal modes, obtained as $I^k = I^k_{HH} + I^k_{HV}$. The blue line is computed by applying a Gaussian broadening of 2 cm^{-1} to the discrete spectrum. For clarity, we only indicate the symmetry of the normal modes with the largest Raman intensities.

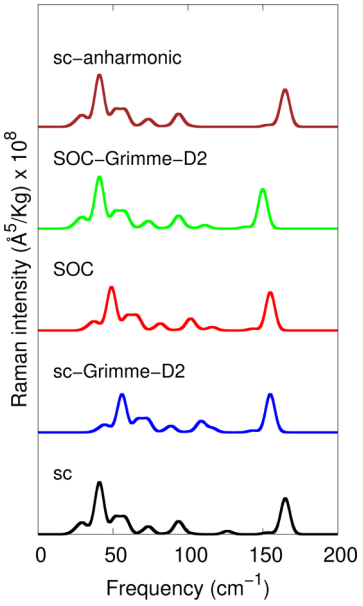

Figure 8. Comparison of the Raman spectra of the orthorhombic $MAPbI_3$ calculated using scalar-relativistic LDA (black) with the spectra obtained after including corrections from vdW interactions (blue), SOC (red), vdW interactions in combination with SOC (green), and anharmonicity (brown).

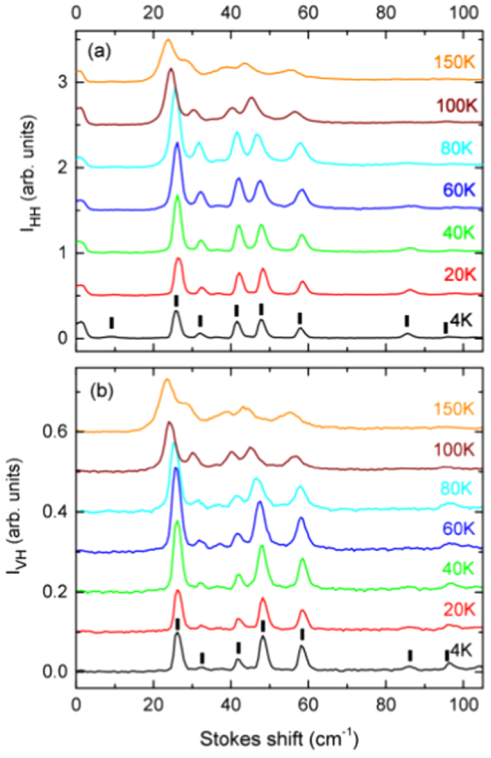

Figure 9. Raman spectra for a single crystal of $MAPbI_3$, measured in backscatter geometry from the (100) plane, using a 830 nm laser polarized (a) parallel (HH) or (b) perpendicular (HV) to the polarization of the scattered light. Spectra acquired at different temperatures are shifted vertically for clarity.

vdW effects and SOC lead to only small changes to the IR intensities[42] and anharmonic renormalization of the intensities can be ruled out on the grounds of molecular dynamics (MD) simulations that yield results similar to ours..[16] Another possible explanation may be lifetime broadening effects, as suggested by Brivio et al.[18] However, Drużbicki et al.[60]

DOI: 10.1021/acs.jpcc.8b04669
J. Phys. Chem. C 2018, 122, 21703−21717

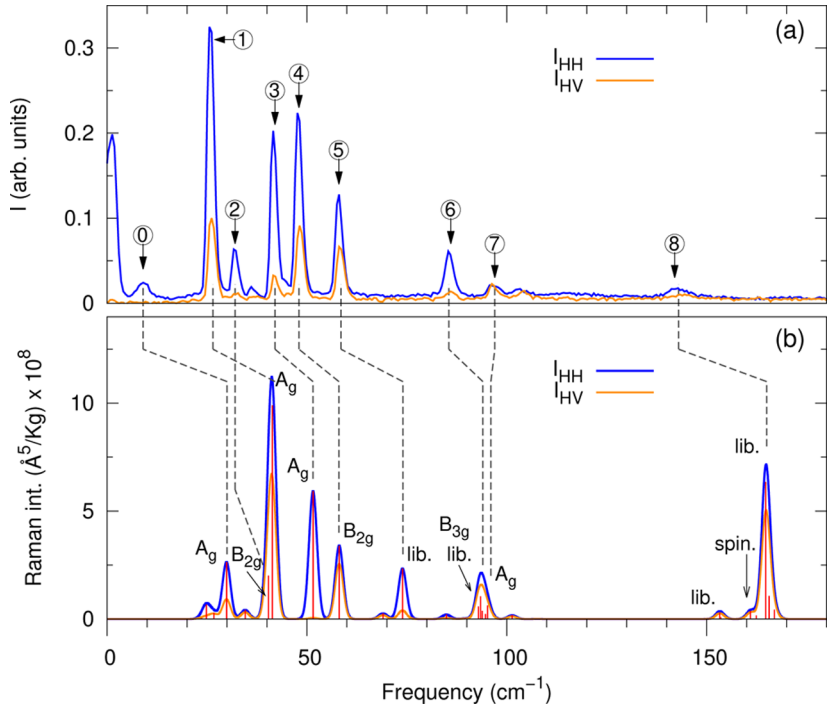

Figure 10. Comparison between the measured (a) and calculated (b) Raman spectra of $MAPbI_3$ in the orthorhombic structure. The experimental spectra are recorded at 4 K. In both panels, the data for the HH and HV configurations are shown in blue and orange, respectively. The red sticks in (b) indicate the calculated Raman intensities for the HH configuration, I_{HH}. The dashed gray lines indicate the tentative assignment of the Raman peaks observed in experiment. In the calculated spectra, we used a Gaussian smearing of 1.0 cm^{-1}.

Table 4. Proposed Assignment of the Main Peaks in the Raman Spectrum of $MAPbI_3$ Acquired at 4 K[a]

peak label	frequency (cm^{-1})	symmetry	description
P_0	9	A_g	Pb−I−Pb rock
P_1	26	A_g	Pb−I−Pb bend
P_2	32	B_{2g}	Pb−I−Pb bend
P_3	42	A_g	Pb−I−Pb bend
P_4	49	B_{2g}	Pb−I−Pb bend
P_5	58		libration/translation
P_6	85	B_{3g}	Pb−I stretch and libration/translation
P_7	97	A_g	Pb−I stretch
P_8	142		libration/translation

[a]The peak labels correspond to those in Figure 10a.

measured the inelastic neutron scattering spectrum of orthorhombic $MAPbI_3$ and found that these modes exhibit considerable intensities, therefore ruling out lifetime broadening effects.

One possibility which is left out of this analysis is the combination of anharmonicity and nuclear quantum effects,[61] which is not captured by the present work and by the MD simulations of ref 16. A thorough investigation of this aspect will require path-integral molecular dynamics simulations,[62] which are computationally prohibitive for a system as complex as $MAPbI_3$.

6. CONCLUSIONS

In summary, we carried out first-principles calculations in conjunction with high-resolution low-temperature Raman measurements to investigate the Raman spectrum of the low-temperature orthorhombic phase of $MAPbI_3$. The good agreement between measured and calculated Raman peaks allowed us to perform a complete assignment of the main peaks observed in the experiments, including the symmetry and character of each normal mode.

We found that the Raman spectrum of $MAPbI_3$ extends up to 3200 cm^{-1} and can be partitioned into three distinct regions: internal vibrations of the MA cations (300−3200 cm^{-1}), libration/translation and spinning of the organic cations (60−180 cm^{-1}), and internal vibrations of the PbI_3 network (0−60 cm^{-1}). For a comparison with experiments, we focused on the low-frequency region. Here, we found that the Raman peaks observed below 50 cm^{-1} correspond to internal vibrations of the inorganic PbI_3 network, whereas the peaks at 58, 85, and 142 cm^{-1} correspond to librational modes of the MA cations (the peak at 85 cm^{-1} also containing a component of PbI_3 vibrations). Our complete assignment is summarized in Table 4 and Figure 10.

The Raman peaks P_1, P_3, P_4, P_5 (at 26, 42, 49, and 58 cm^{-1}) are intense and well separated; therefore, they could be used as markers for monitoring of the $MAPbI_3$ structure and stoichiometry. In particular, the P_1, P_3, and P_4 peaks can clearly be identified with vibrations of the PbI_3 network, whereas the P_5 peak comes from the MA cations. Therefore, we suggest that the ratios of the intensities P_1/P_5, P_3/P_5, and P_4/P_5 could be used to monitor the PbI_2/MAI ratio in the system, for example, to detect deviations from the ideal stoichiometry or to monitor degradation.

We observed a discrepancy between theory and experiment for the P_8 peak, which corresponds to librational/translational modes of MA. In this case, the calculations yield a too strong Raman intensity, and the effect is analogous to what was previously observed for IR spectra.[34] We ruled out vdW effects, SOC, and anharmonicity as the origin of this discrepancy, and

DOI: 10.1021/acs.jpcc.8b04669
J. Phys. Chem. C 2018, 122, 21703−21717

we proposed that path-integral MD simulations might be necessary to clarify this aspect.

Overall, we reported the first complete assignment of the symmetry and character of the main Raman peaks of orthorhombic $MAPbI_3$ in the low-frequency range. We hope that the present study will serve as a solid framework for future characterization of this important organic−inorganic perovskite.

APPENDIX A

The Raman tensors of the orthorhombic $MAPbI_3$ (*Pnma*) have the following symmetries

Table 5. Predicted Raman Activity of the Normal Modes in Orthorhombic $MAPbI_3$, for Several Backscattering Geometries[a]

backscattering geometry	normal mode symmetry			
	A_g	B_{1g}	B_{2g}	B_{3g}
$x(yy)\bar{x}$	R			
$x(zz)\bar{x}$	R			
$x(yz)\bar{x}$				R
$x(y'y')\bar{x}$	R			R
$x(z'z')\bar{x}$	R			R
$x(y'z')\bar{x}$	R			
$y(xx)\bar{y}$	R			
$y(zz)\bar{y}$	R			
$y(xz)\bar{y}$			R	
$y(x''x'')\bar{y}$	R		R	
$y(z''z'')\bar{y}$	R		R	
$y(x''z'')\bar{y}$	R			

[a] x, y, and z denote the [100], [010], and [001] crystallographic directions in the orthorhombic unit cell of $MAPbI_3$, respectively. y', z', x'', and z'' indicate the [011], [0$\bar{1}$1], [101], and [$\bar{1}$01] crystallographic directions, respectively, and R denotes nonzero Raman activity.

$$\bar{\alpha}(A_g) = \begin{pmatrix} a & 0 & 0 \\ 0 & b & 0 \\ 0 & 0 & c \end{pmatrix}, \quad \bar{\alpha}(B_{1g}) = \begin{pmatrix} 0 & d & 0 \\ d & 0 & 0 \\ 0 & 0 & 0 \end{pmatrix}$$

$$\bar{\alpha}(B_{2g}) = \begin{pmatrix} 0 & 0 & e \\ 0 & 0 & 0 \\ e & 0 & 0 \end{pmatrix}, \quad \bar{\alpha}(B_{3g}) = \begin{pmatrix} 0 & 0 & 0 \\ 0 & 0 & f \\ 0 & f & 0 \end{pmatrix}$$

Making use of the symmetry of the Raman tensors and eq 1 of the main text (that is, $I^k \propto \frac{1}{\omega_k}|\mathbf{e}_i \cdot \bar{\alpha}^k \cdot \mathbf{e}_s|^2$), we predict the Raman activity of the normal modes for several orientations of a single crystal of $MAPbI_3$, in backscattering geometry $\mathbf{k}_i(\mathbf{e}_i, \mathbf{e}_s)\mathbf{k}_s$, with $\mathbf{k}_i = -\mathbf{k}_s \cdot \mathbf{k}_i$ and $\mathbf{k}_s$ are the directions of the propagation vectors of the incoming and scattered photons, respectively, and $\mathbf{e}_i$ and $\mathbf{e}_s$ are their corresponding polarization vectors. The backscattering geometries considered here and the predicted Raman activity of the normal modes are shown in Table 5.

To confirm our predictions, we explicitly calculate the Raman intensities of the normal modes by solving eq 1 for the following backscattering geometries $x(yy)\bar{x}$, $x(yz)\bar{x}$, $y(xx)\bar{y}$, and $y(xz)\bar{y}$. With the resulting Raman intensities, we calculate the corresponding Raman spectra, and our results are shown in Figure 11c,d. In this figure, we also compare the spectra with the calculated Raman spectra using the isotropic average and with experiment.

As one can see, the A_g normal modes observed in the calculated Raman spectra using the isotropic average (Figure 11b) exhibit nonzero Raman intensities in the backscattering geometries $x(yy)\bar{x}$ and $y(xx)\bar{y}$. On the contrary, the B_{1g}, B_{2g}, and B_{3g} normal modes observed in Figure 11b vanish in these backscattering configurations. These observations are in line with our symmetry-based predictions. In the case of the calculated Raman spectra for the configurations $x(yz)\bar{x}$ and $y(xz)\bar{y}$ (Figure 11c), we observe that the B_{3g} and B_{2g} normal modes show nonzero Raman intensities, respectively, whereas the A_g modes do not. This result is also in line with our symmetry-based predictions.

As one can see, the calculated Raman spectra of Figure 11b,c strongly depend on the backscattering configuration. This analysis reveals that although the geometry modifies the intensity of the peaks as expected, the intensity of the peak P_8 remains large irrespective of the geometry.

Overall, the results presented in this Appendix could be useful to experimentalists for characterizing the Raman spectra of orthorhombic $MAPbI_3$ measured on a single crystal and to demonstrate the symmetry of the lattice vibrations in this system.

AUTHOR INFORMATION

Corresponding Author

*E-mail: feliciano.giustino@materials.ox.ac.uk.

ORCID

Miguel A. Pérez-Osorio: 0000-0001-8077-5655
Laura M. Herz: 0000-0001-9621-334X
Michael B. Johnston: 0000-0002-0301-8033
Feliciano Giustino: 0000-0001-9293-1176

Notes

The authors declare no competing financial interest.

ACKNOWLEDGMENTS

The research leading to these results has received funding from the Leverhulme Trust (Grant RL-2012-001), the U.K. Engineering and Physical Sciences Research Council (Grant Nos. EP/M020517/1, EP/P006329/1, EP/L024667/1), the EU Horizon 2020 INFORM ITN (Grant No. 675867), and the Graphene Flagship (Horizon 2020 Grant No. 785219 - GrapheneCore2). The authors acknowledge the use of the University of Oxford Advanced Research Computing (ARC) facility (http://dx.doi.org/10.5281/zenodo.22558); the ARCHER U.K. National Supercomputing Service under the "T-Dops" project; the DECI resource "Cartesius" based in The Netherlands at SURFsara and "Abel" based in Oslo with support from the PRACE AISBL; PRACE for awarding us access to MareNostrum at BSC-CNS, Spain; CSD3, U.K. EPSRC (Grant No. EP/P020259/1). All structural models were rendered using VESTA.[63]

REFERENCES

(1) Snaith, H. J. Present Status and Future Prospects of Perovskite Photovoltaics. *Nat. Mater.* **2018**, *17*, 372−376.

(2) Lee, M. M.; Teuscher, J.; Miyasaka, T.; Murakami, T. N.; Snaith, H. J. Efficient Hybrid Solar Cells Based on Meso-Superstructured Organometal Halide Perovskites. *Science* **2012**, *338*, 643−647.

(3) Green, M. A.; Ho-Baillie, A. Perovskite Solar Cells: The Birth of a New Era in Photovoltaics. *ACS Energy Lett.* **2017**, *2*, 822−830.

DOI: 10.1021/acs.jpcc.8b04669
J. Phys. Chem. C 2018, 122, 21703−21717

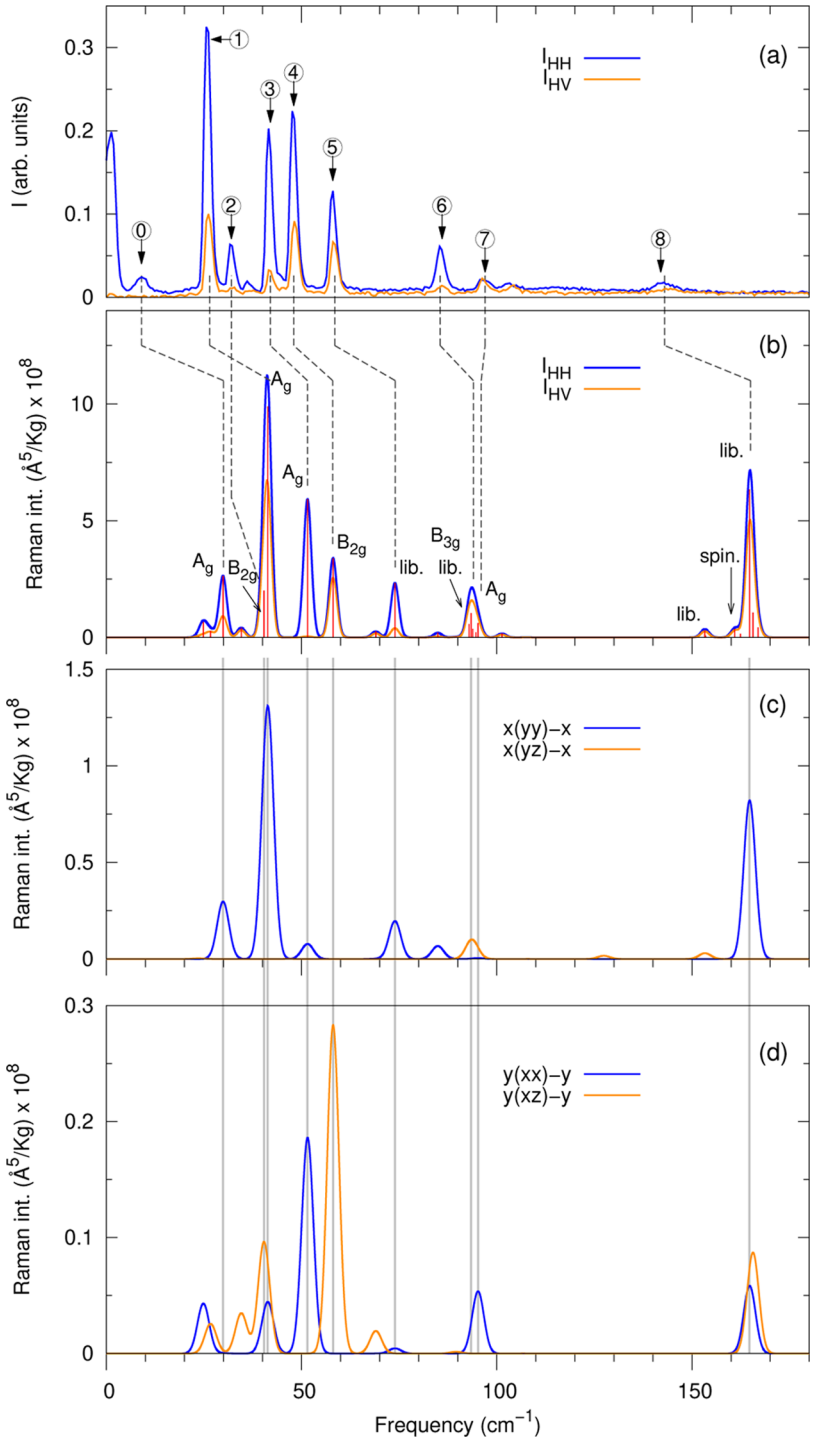

Figure 11. Measured and calculated Raman spectra of orthorhombic $MAPbI_3$. (a) Measured Raman spectra at 4 K, in HH and HV backscattering polarization configurations. (b) Calculated Raman spectra in HH and HV polarization configurations, using the isotropic average (see Section 2 for further details). (c) Calculated Raman spectra for the backscattering geometries $x(yy)\bar{x}$ and $x(yz)\bar{x}$. (d) Calculated Raman spectra for the backscattering geometries $y(xx)\bar{y}$ and $y(xz)\bar{y}$. Panels (a) and (b) are the same as in Figure 10. The vertical light gray lines are guides to the eye, to indicate the frequencies of the normal modes with the highest Raman intensities in (b).

(4) Eperon, G. E.; Leijtens, T.; Bush, K. A.; Prasanna, R.; Green, T.; Wang, J. T.-W.; McMeekin, D. P.; Volonakis, G.; Milot, R. L.; May, R.; et al. Perovskite-perovskite Tandem Photovoltaics with Optimized Bandgaps. *Science* **2016**, 861−865.

(5) Liu, M.; Johnston, M. B.; Snaith, H. J. Efficient Planar Heterojunction Perovskite Solar Cells by Vapour Deposition. *Nature* **2013**, *501*, 395−398.

(6) Baikie, T.; Fang, Y.; Kadro, J. M.; Schreyer, M.; Wei, F.; Mhaisalkar, S. G.; Graetzel, M.; White, T. J. Synthesis and Crystal Chemistry of the Hybrid Perovskite $CH_3NH_3PbI_3$ for Solid-State Sensitised Solar Cell Applications. *J. Mater. Chem. A* **2013**, *1*, 5628−5641.

(7) Weller, M. T.; Weber, O. J.; Henry, P. F.; Pumpo, A. M. D.; Hansen, T. C. Complete Structure and Cation Orientation in the

DOI: 10.1021/acs.jpcc.8b04669
J. Phys. Chem. C 2018, 122, 21703−21717

Perovskite Photovoltaic Methylammonium Lead Iodide between 100 and 352 K. *Chem. Commun.* **2015**, *51*, 4180−4183.
(8) Whitfield, P. S.; Herron, N.; Guise, W. E.; Page, K.; Cheng, Y. Q.; Milas, I.; Crawford, M. K. Structures, Phase Transitions and Tricritical Behavior of the Hybrid Perovskite Methyl Ammonium Lead Iodide. *Sci. Rep.* **2016**, *6*, No. 35685.
(9) Quarti, C.; Mosconi, E.; Ball, J. M.; D'Innocenzo, V.; Tao, C.; Pathak, S.; Snaith, H. J.; Petrozza, A.; Angelis, F. D. Structural and Optical Properties of Methylammonium Lead Iodide Across the Tetragonal to Cubic Phase Transition: Implications for Perovskite Solar Cells. *Energy Environ. Sci.* **2016**, *9*, 155−163.
(10) Davies, C. L.; Filip, M. R.; Patel, J. B.; Crothers, T. W.; Verdi, C.; Wright, A. D.; Milot, R. L.; Giustino, F.; Johnston, M. B.; Herz, L. M. Bimolecular Recombination in Methylammonium Lead Triiodide Perovskite Is an Inverse Absorption Process. *Nat. Commun.* **2018**, *9*, No. 293.
(11) Wehrenfennig, C.; Eperon, G. E.; Johnston, M. B.; Snaith, H. J.; Herz, L. M. High Charge Carrier Mobilities and Lifetimes in Organolead Trihalide Perovskites. *Adv. Mater.* **2014**, *26*, 1584.
(12) Stoumpos, C. C.; Malliakas, C. D.; Kanatzidis, M. G. Semiconducting Tin and Lead Iodide Perovskites with Organic Cations: Phase Transitions, High Mobilities, and Near-Infrared Photoluminescent Properties. *Inorg. Chem.* **2013**, *52*, 9019−9038.
(13) Herz, L. M. Charge-Carrier Mobilities in Metal Halide Perovskites: Fundamental Mechanisms and Limits. *ACS Energy Lett.* **2017**, *2*, 1539−1548.
(14) Maalej, A.; Abid, Y.; Kallel, A.; Daoud, A.; Lautié, A.; Romain, F. Phase Transitions and Crystal Dynamics in the Cubic Perovskite $CH_3NH_3PbCl_3$. *Solid State Commun.* **1997**, *103*, 279−284.
(15) Grancini, G.; Marras, S.; Prato, M.; Giannini, C.; Quarti, C.; De Angelis, F.; De Bastiani, M.; Eperon, G. E.; Snaith, H. J.; Manna, L.; et al. The Impact of the Crystallization Processes on the Structural and Optical Properties of Hybrid Perovskite Films for Photovoltaics. *J. Phys. Chem. Lett.* **2014**, *5*, 3836−3842.
(16) Quarti, C.; Grancini, G.; Mosconi, E.; Bruno, P.; Ball, J. M.; Lee, M. M.; Snaith, H. J.; Petrozza, A.; De Angelis, F. The Raman Spectrum of the $CH_3NH_3PbI_3$ Hybrid Perovskite: Interplay of Theory and Experiment. *J. Phys. Chem. Lett.* **2014**, *5*, 279−284.
(17) Ledinský, M.; Löper, P.; Niesen, B.; Holovský, J.; Moon, S.-J.; Yum, J.-H.; De Wolf, S.; Fejfar, A.; Ballif, C. Raman Spectroscopy of Organic-Inorganic Halide Perovskites. *J. Phys. Chem. Lett.* **2015**, *6*, 401−406.
(18) Brivio, F.; Frost, J. M.; Skelton, J. M.; Jackson, A. J.; Weber, O. J.; Weller, M. T.; Goñi, A. R.; Leguy, A. M. A.; Barnes, P. R. F.; Walsh, A. Lattice Dynamics and Vibrational Spectra of the Orthorhombic, Tetragonal, and Cubic Phases of Methylammonium Lead Iodide. *Phys. Rev. B* **2015**, *92*, No. 144308.
(19) Glaser, T.; Müller, C.; Sendner, M.; Krekeler, C.; Semonin, O. E.; Hull, T. D.; Yaffe, O.; Owen, J. S.; Kowalsky, W.; Pucci, A.; et al. Infrared Spectroscopic Study of Vibrational Modes in Methylammonium Lead Halide Perovskites. *J. Phys. Chem. Lett.* **2015**, 2913−2918.
(20) Wright, A. D.; Verdi, C.; Milot, R. L.; Eperon, G. E.; Pérez-Osorio, M. A.; Snaith, H. J.; Giustino, F.; Johnston, M. B.; Herz, L. M. Electron-phonon Coupling in Hybrid Lead Halide Perovskites. *Nat. Commun.* **2016**, *7*, No. 11755.
(21) Herz, L. M. Charge-Carrier Dynamics in Organic-Inorganic Metal Halide Perovskites. *Annu. Rev. Phys. Chem.* **2016**, *67*, 65−89.
(22) Umari, P.; Mosconi, E.; De Angelis, F. Infrared Dielectric Screening Determines the Low Exciton Binding Energy of Metal-Halide Perovskites. *J. Phys. Chem. Lett.* **2018**, *9*, 620−627.
(23) Kirchartz, T.; Markvart, T.; Rau, U.; Egger, D. A. Impact of Small Phonon Energies on the Charge-Carrier Lifetimes in Metal-Halide Perovskites. *J. Phys. Chem. Lett.* **2018**, *9*, 939−946.
(24) Yu, X.; Qin, Y.; Peng, Q. Probe Decomposition of Methylammonium Lead Iodide Perovskite in N_2 and O_2 by in Situ Infrared Spectroscopy. *J. Phys. Chem. A* **2017**, *121*, 1169−1174.
(25) Capitani, F.; Marini, C.; Caramazza, S.; Dore, P.; Pisanu, A.; Malavasi, L.; Nataf, L.; Baudelet, F.; Brubach, J.-B.; Roy, P.; et al. Locking of Methylammonium by Pressure-Enhanced H-Bonding in $(CH_3NH_3)PbBr_3$ Hybrid Perovskite. *J. Phys. Chem. C* **2017**, *121*, 28125−28131.
(26) Létoublon, A.; Paofai, S.; Rufflé, B.; Bourges, P.; Hehlen, B.; Michel, T.; Ecolivet, C.; Durand, O.; Cordier, S.; Katan, C.; et al. Elastic Constants, Optical Phonons, and Molecular Relaxations in the High Temperature Plastic Phase of the $CH_3NH_3PbBr_3$ Hybrid Perovskite. *J. Phys. Chem. Lett.* **2016**, 3776−3784.
(27) Yu, P. Y.; Cardona, M. *Fundamentals of Semiconductors. Physics and Materials Properties*; Springer-Verlag: Berlin, 1996.
(28) Iliev, M. N.; Abrashev, M. V.; Lee, H.-G.; Popov, V. N.; Sun, Y. Y.; Thomsen, C.; Meng, R. L.; Chu, C. W. Raman Spectroscopy of Orthorhombic Perovskitelike $YMnO_3$ and $LaMnO_3$. *Phys. Rev. B* **1998**, *57*, 2872−2877.
(29) Pistor, P.; Ruiz, A.; Cabot, A.; Izquierdo-Roca, V. Advanced Raman Spectroscopy of Methylammonium Lead Iodide: Development of a Non-destructive Characterisation Methodology. *Sci. Rep.* **2016**, *6*, No. 35973.
(30) Li, D.; Wang, G.; Cheng, H.-C.; Chen, C.-Y.; Wu, H.; Liu, Y.; Huang, Y.; Duan, X. Size-dependent Phase Transition in Methylammonium Lead Iodide Perovskite Microplate Crystals. *Nat. Commun.* **2016**, *7*, No. 11330.
(31) Guo, Y.; Yaffe, O.; Paley, D. W.; Beecher, A. N.; Hull, T. D.; Szpak, G.; Owen, J. S.; Brus, L. E.; Pimenta, M. A. Interplay between Organic Cations and Inorganic Framework and Incommensurability in Hybrid Lead-halide Perovskite $CH_3NH_3PbBr_3$. *Phys. Rev. Mater.* **2017**, *1*, No. 042401.
(32) Dove, M. T. *Structure and Dynamics. An Atomic View of Materials*; Oxford University Press: Oxford, 2012.
(33) Abdelmageed, G.; Jewell, L.; Hellier, K.; Seymour, L.; Luo, B.; Bridges, F.; Zhang, J. Z.; Carter, S. Mechanisms for Light Induced Degradation in $MAPbI_3$ Perovskite Thin Films and Solar Cells. *Appl. Phys. Lett.* **2016**, *109*, No. 233905.
(34) Pérez-Osorio, M. A.; Milot, R. L.; Filip, M. R.; Patel, J. B.; Herz, L. M.; Johnston, M. B.; Giustino, F. Vibrational Properties of the Organic-Inorganic Halide Perovskite $CH_3NH_3PbI_3$ from Theory and Experiment: Factor Group Analysis, First-Principles Calculations, and Low-Temperature Infrared Spectra. *J. Phys. Chem. C* **2015**, *119*, 25703−25718.
(35) Sendner, M.; Nayak, P. K.; Egger, D. A.; Beck, S.; Müller, C.; Epding, B.; Kowalsky, W.; Kronik, L.; Snaith, H. J.; Pucci, A.; et al. Optical Phonons in Methylammonium Lead Halide Perovskites and Implications for Charge Transport. *Mater. Horiz.* **2016**, *3*, 613−620.
(36) Schuck, G.; Többens, D. M.; Koch-Müller, M.; Efthimiopoulos, I.; Schorr, S. Infrared Spectroscopic Study of Vibrational Modes across the Orthorhombic-Tetragonal Phase Transition in Methylammonium Lead Halide Single Crystals. *J. Phys. Chem. C* **2018**, *122*, 5227−5237.
(37) Zhou, Y.; Garces, H. F.; Padture, N. P. Challenges in the Ambient Raman Spectroscopy Characterization of Methylammonium Lead Triiodide Perovskite Thin Films. *Front. Optoelectron.* **2016**, *9*, 81−86.
(38) Leguy, A. M. A.; Goñi, A. R.; Frost, J. M.; Skelton, J.; Brivio, F.; Rodrìguez-Martìnez, X.; Weber, O. J.; Pallipurath, A.; Isabel Alonso, M.; Campoy-Quiles, M.; et al. Dynamic Disorder, Phonon Lifetimes, and the Assignment of Modes to the Vibrational Spectra of Methylammonium Lead Halide Perovskites. *Phys. Chem. Chem. Phys.* **2016**, *18*, 27051−27066.
(39) Mattoni, A.; Filippetti, A.; Saba, M.; Caddeo, C.; Delugas, P. Temperature Evolution of Methylammonium Trihalide Vibrations at the Atomic Scale. *J. Phys. Chem. Lett.* **2016**, *7*, 529−535.
(40) Saidaminov, M. I.; Abdelhady, A. L.; Murali, B.; Alarousu, E.; Burlakov, V. M.; Peng, W.; Dursun, I.; Wang, L.; He, Y.; Maculan, G.; et al. High-quality Bulk Hybrid Perovskite Single Crystals within Minutes by Inverse Temperature Crystallization. *Nat. Commun.* **2015**, *6*, No. 7586.
(41) Giannozzi, P.; Andreussi, O.; Brumme, T.; Bunau, O.; Nardelli, M. B.; Calandra, M.; Car, R.; Cavazzoni, C.; Ceresoli, D.; Cococcioni, M.; et al. Advanced Capabilities for Materials Modelling with

DOI: 10.1021/acs.jpcc.8b04669
J. Phys. Chem. C 2018, 122, 21703−21717

Quantum ESPRESSO. *J. Phys.: Condens. Matter* **2017**, *29*, No. 465901.
(42) Pérez-Osorio, M. A.; Champagne, A.; Zacharias, M.; Rignanese, G.-M.; Giustino, F. Van der Waals Interactions and Anharmonicity in the Lattice Vibrations, Dielectric Constants, Effective Charges, and Infrared Spectra of the Organic-Inorganic Halide Perovskite $CH_3NH_3PbI_3$. *J. Phys. Chem. C* **2017**, *121*, 18459−18471.
(43) Perdew, J. P.; Burke, K.; Ernzerhof, M. Generalized Gradient Approximation Made Simple. *Phys. Rev. Lett.* **1996**, *77*, 3865−3868.
(44) Ceperley, D. M.; Alder, B. J. Ground State of the Electron Gas by a Stochastic Method. *Phys. Rev. Lett.* **1980**, *45*, 566−569.
(45) Troullier, N.; Martins, J. L. Efficient Pseudopotentials for Plane-Wave Calculations. *Phys. Rev. B* **1991**, *43*, 1993−2006.
(46) Umari, P.; Pasquarello, A. First-principles Analysis of the Raman Spectrum of Vitreous Silica: Comparison with the Vibrational Density of States. *J. Phys.: Condens. Matter* **2003**, *15*, S1547.
(47) Kauschke, W.; Cardona, M. Resonant Raman Scattering and Interference Effects of LO Phonons at the $E_0 + \Delta_0$ Gap of InP. *Phys. Rev. B* **1986**, *33*, 5473−5481.
(48) Kauschke, W.; Cardona, M.; Bauser, E. Resonant Raman Scattering by LO Phonons in $Al_xGa_{1-x}As$ ($x < 0.1$): Alloying and Interference Effects. *Phys. Rev. B* **1987**, *35*, 8030−8041.
(49) Lukačević, I.; Gupta, S. K.; Jha, P. K.; Kirin, D. Lattice dynamics and Raman Spectrum of Rutile TiO_2: The Role of Soft Phonon Modes in Pressure Induced Phase Transition. *Mater. Chem. Phys.* **2012**, *137*, 282−289.
(50) Umari, P.; Pasquarello, A.; Dal Corso, A. Raman Scattering Intensities in α-quartz: A First-Principles Investigation. *Phys. Rev. B* **2001**, *63*, No. 094305.
(51) Grimme, S. Semiempirical GGA-type Density Functional Constructed with a Long-range Dispersion Correction. *J. Comput. Chem.* **2006**, *27*, 1787−1799.
(52) Barone, V.; Casarin, M.; Forrer, D.; Pavone, M.; Sambi, M.; Vittadini, A. Role and Effective Treatment of Dispersive Forces in Materials: Polyethylene and Graphite Crystals as Test Cases. *J. Comput. Chem.* **2009**, *30*, 934−939.
(53) Rousseau, D. L.; Bauman, R. P.; Porto, S. P. S. Normal Mode Determination in Crystals. *J. Raman Spectrosc.* **1981**, *10*, 253−290.
(54) Aroyo, M. I.; Perez-Mato, J. M.; Capillas, C.; Kroumova, E.; Ivantchev, S.; Madariaga, G.; Kirov, A.; Wondratschek, H. Bilbao Crystallographic Server: I. Databases and crystallographic computing programs. *Z. Kristallogr. - Cryst. Mater.* **2009**, *221*, 15−27.
(55) Aroyo, M. I.; Perez-Mato, J.; Orobengoa, D.; Tasci, E.; De, L. F.; Kirov, A. Crystallography Online: Bilbao Crystallographic Server. *Bulg. Chem. Commun.* **2011**, *43*, 183−197.
(56) Islam, M. A.; Rondinelli, J. M.; Spanier, J. E. Normal Mode Determination of Perovskite Crystal Structures with Octahedral Rotations: Theory and Applications. *J. Phys.: Condens. Matter* **2013**, *25*, No. 175902.
(57) Champagne, A. Vibrational Properties of Hybrid Halide Perovskite for Solar Cells Applications. Master thesis; Ecole polytechnique de Louvain, Université catholique de Louvain, 2016.
(58) Mattoni, A.; Filippetti, A.; Saba, M. I.; Delugas, P. Methylammonium Rotational Dynamics in Lead Halide Perovskite by Classical Molecular Dynamics: The Role of Temperature. *J. Phys. Chem. C* **2015**, *119*, 17421−17428.
(59) Mattoni, A.; Filippetti, A.; Caddeo, C. Modeling Hybrid Perovskites by Molecular Dynamics. *J. Phys.: Condens. Matter* **2017**, *29*, No. 043001.
(60) Drużbicki, K.; Pinna, R. S.; Rudic, S.; Jura, M.; Gorini, G.; Fernandez-Alonso, F. Unexpected Cation Dynamics in the Low-Temperature Phase of Methylammonium Lead Iodide: The Need for Improved Models. *J. Phys. Chem. Lett.* **2016**, *7*, 4701−4709.
(61) Patrick, C. E.; Giustino, F. Quantum Nuclear Dynamics in the Photophysics of Diamondoids. *Nat. Commun.* **2013**, *4*, No. 2006.
(62) Marx, D.; Parrinello, M. Ab Initio Path Integral Molecular Dynamics: Basic Ideas. *J. Chem. Phys.* **1996**, *104*, 4077−4082.
(63) Momma, K.; Izumi, F. VESTA : a Three-Dimensional Visualization System for Electronic and Structural Analysis. *J. Appl. Crystallogr.* **2008**, 653−658.

DOI: 10.1021/acs.jpcc.8b04669
J. Phys. Chem. C 2018, 122, 21703−21717